



Numerical Modeling of Plasma Formation in Hypersonic Flow: A **Comparative Study of Thermochemical Models**

Luigi Cutrone¹, Salvatore Esposito², Antonio Schettino³, Domenic D'Ambrosio⁴

Abstract

Plasma formation in hypersonic reentry flows affects electromagnetic wave propagation, with direct implications for vehicle communications and radar signature. Accurate prediction of ionization is therefore essential to quantify these effects. This work presents a numerical analysis of electron density under the examined flight conditions of the RAM-C II vehicle using the in-house solver NExT, compared against CFD++ results and flight measurements. The simulations solve the compressible Navier-Stokes equations for a multicomponent, chemically reacting air mixture in thermal and chemical nonequilibrium, incorporating a multi-temperature model for vibrational energy. The influence of chemical kinetics, vibrational-chemical coupling, and surface catalyticity is systematically assessed. Among the tested kinetic schemes, Park'85 consistently overestimates electron concentrations, whereas Park'93 and Kim achieve closer agreement with experimental data. Surface boundary conditions also affect results, with a hybrid approach—non-catalytic for neutral species and catalytic for charged species—producing the most consistent match with experimental data. Differences between NExT and CFD++ are most pronounced at the lowest and highest altitudes, whereas chemical kinetics and wall treatments affect electron density predictions across the examined flight conditions. The study provides a quantitative evaluation of modeling assumptions in hypersonic plasma simulations, supporting the application of NExT to reentry flow analyses where plasma-electromagnetic interactions are relevant.

Keywords: Aerothermodynamics, Ionization, Non-equilibrium, Chemical Kinetics

Nomenclature

Latin T_{e} Electron temperature Mass fraction C Molar concentration Greek *D* − Diffusion coefficient e_V – Vibrational energy δ - Greek symbol - Specific enthalpy of species k- Density ρ θ^v Δh^0 – Formation enthalpy k_f – Forward reaction rate $\dot{\omega}$ Backward reaction rate Superscripts K_{eq} – Chemical equilibrium constant

M - Molar mass - Pressure pHeat flux

 Q_{VT} – Vibrational–translational energy exchange

 Q_D – Vibrational energy loss due to dissociation S_{ij} – Strain rate tensor component

Translational—rotational temperature

 T_V – Vibrational temperature

Characteristic vibrational temperatue

Chemical production rate

- Reactant stoichiometric coefficient - Product stoichiometric coefficient

Subscripts

f- Backward f Forward

- Chemical species index k- Reaction index

¹Italian Aerospace Research Center, l.cutrone@cira.it

²Italian Aerospace Research Center, s.esposito@cira.it

³Italian Aerospace Research Center, a.schettino@cira.it

⁴Politecnico di Torino, domenic.dambrosio@polito.it

1. Introduction

Accurate prediction of ionization in hypersonic flows is essential for characterizing the plasma environment encountered by reentry vehicles. Shock-induced compression and heating trigger high-temperature reactions that, under appropriate conditions, generate a partially ionized gas capable of altering electromagnetic wave propagation [25]. These effects have direct consequences for communications [2] and radar signature of the vehicle [24, 6]. Modeling such phenomena requires numerical tools that resolve a compressible, chemically reacting mixture in thermal and chemical non-equilibrium, where the electron density plays a central role in defining plasma behavior. A validated computational framework is therefore critical for reliably quantifying these properties.

Building on such a framework, the present study assesses the sensitivity of an in-house CFD solver to thermochemical parameters through application to the RAM-C II test case [8]. The analysis focuses on how different kinetic schemes, as well as wall and flight conditions, affect the prediction of electron concentrations during hypersonic flight. Although the RAM-C II configuration is a standard benchmark for validation, few works have systematically examined the influence of modeling choices on electron density predictions. This study addresses that gap by evaluating the solver's robustness to thermochemical uncertainties and its capability to capture ionization phenomena. The numerical results are compared with independent CFD++ results [5], providing an external reference for accuracy assessment. This approach enhances confidence in numerical modeling of hypersonic plasmas and contributes to the development of reliable predictive tools for the design and operation of reentry vehicles.

2. Governing Equations

The flow is modeled by the Navier–Stokes equations for a compressible, viscous, chemically reacting gas mixture with multiple components, in a state of thermal and chemical nonequilibrium. The equations describe the evolution of species mass fractions Y_k , velocity u_i , pressure p, density ρ , and total energy E. In differential form, the equations are [1]:

$$\frac{\partial}{\partial t} (\rho Y_k) + \frac{\partial}{\partial x_i} (\rho Y_k u_j) + \frac{\partial}{\partial x_i} (J_{k,j}) = \omega_k, \tag{1}$$

$$\frac{\partial}{\partial t} (\rho u_i) + \frac{\partial}{\partial x_j} (\rho u_i u_j) + \frac{\partial}{\partial x_j} (\rho \delta_{ij} - \sigma_{ij}) = 0,$$
(2)

$$\frac{\partial}{\partial t} (\rho E) + \frac{\partial}{\partial x_j} \left[\rho u_j \left(E + \frac{p}{\rho} \right) \right] + \frac{\partial}{\partial x_j} (-q_j - u_i \sigma_{ij}) = 0.$$
 (3)

where

$$E = e_{\mathsf{int}} + \sum_{k} Y_k \Delta h_k^0 + \frac{1}{2} u_i u_i \tag{4}$$

$$J_{k,j} = -\rho D_k \frac{\partial Y_k}{\partial x_j}, \qquad q_j = -(\eta_{\mathsf{tr}} + \eta_{\mathsf{rot}}) \frac{\partial T}{\partial x_j} - \eta_V \frac{\partial T_{V,k}}{\partial x_j} - \sum_k \rho h_k D_k \frac{\partial Y_k}{\partial x_j}, \tag{5}$$

$$\sigma_{ij} = 2\mu S_{ij} - \frac{2}{3}\mu S_{ll}\delta_{ij}, \qquad S_{ij} = \frac{1}{2}\left(\frac{\partial u_i}{\partial x_j} + \frac{\partial u_j}{\partial x_i}\right).$$
 (6)

(7)

Here, ω_k and Δh_k^0 are, respectively, the average reaction rate production and the enthalpy of formation of species k.

The mean pressure p is determined from the state equation:

$$p = \rho T \sum_{k} Y_k R_k. \tag{8}$$

2.1. Thermal nonequilibrium

In the multi-temperatures model, the vibrational energy is treated as a nonequilibrium energy mode, and the energy conservation equation of the vibrational energy for the k-th molecular species is

$$\frac{\partial}{\partial t}(\rho e_{V,k}) + \frac{\partial}{\partial x_j}(\rho e_{V,k}u_j) = \frac{\partial}{\partial x_j}\left(\eta_{V,k}\frac{\partial T_{V,k}}{\partial x_j}\right) + \frac{\partial}{\partial x_j}\left(h_{v,s}D_s\frac{\partial Y_k}{\partial x_j}\right) + \dot{\omega}_{V,k},\tag{9}$$

Where $e_{V,k}$, $\eta_{V,k}$, and $T_{V,k}$ are the specific energy, thermal conductivity, and temperature of the vibrational energy mode, respectively. $h_{V,k}$ and D_k are the specific enthalpy and diffusion coefficient. In Eq. 9, the source term $\dot{\omega}_{V,k}$ is expressed as

$$\dot{\omega}_{V,k} = Q^{VT,k} + Q_{D,k},\tag{10}$$

where $Q_{V-T,k}$ is the rate of internal energy transfer in the vibrational-to-translational (V-T) process, and $Q_{D,k}$ is the vibrational energy losses due to heavy-particle and electron impact dissociation, for each molecular species k.

For the V-T energy transfer (Q^{VT}), the Landau–Teller model [11] has been widely used:

$$Q_{VT,k} = \frac{\rho_k \left(e_{V,k}^* - e_{V,k} \right)}{\tau_k^{VT}},\tag{11}$$

where ρ_k is species density, $e_{V,k}^*$ and $e_{V,k}$ are the vibrational equilibrium and nonequilibrium energy per unit mass of molecular species k, respectively. The characteristic vibrational relaxation time of a species τ_k^{VT} is expressed in terms of binary relaxation times τ_{kj} . These are functions of pressure and temperature and can be estimated with the Millikan-White formula [12]:

$$\tau_{kj} = \exp\left[0.00116\left(T^{-1/3} - 0.015\mu_{kj}^{1/4}\right) - 18.42\right] \frac{1}{p}.$$
 (12)

For vibrational energy losses due to the heavy-particle and electron collisions term Q_D in Eq. 10, the preferential dissociation model [17, 15] (i.e., a molecule is more likely to dissociate if it is in a higher vibrational state and atoms that recombine are more likely to create molecules in a higher vibrational state) in the vibrational energy conservation yields to:

$$Q_{D,k} = \hat{c}_1 \dot{\omega}_k D_{s,k},\tag{13}$$

where $D_{s,k}$ is the bond dissociation energy for molecular species k and \hat{c}_1 is a constant less than 1, here equal to 0.3 according to the work of Sharma, Huo, and Park [23].

2.2. Chemical nonequilibrium

The mixture composition does not adjust instantaneously but evolves over a characteristic relaxation scale, which defines the regime of chemical non-equilibrium. The chemical source term $\dot{\omega}_k$ appearing in Eq. (1) is evaluated via the law of mass action as

$$\dot{\omega}_{k} = \mathcal{M}_{k} \sum_{r=1}^{N_{r}} \left(\nu_{k,r}^{"} - \nu_{k,r}^{'} \right) \left(k_{f,r} \prod_{i=1}^{N_{s}} C_{i}^{\nu_{i,r}^{'}} - k_{b,r} \prod_{i=1}^{N_{s}} C_{i}^{\nu_{i,r}^{"}} \right), \tag{14}$$

where \mathcal{M}_k is the molar mass of species k, $\nu'_{i,r}$ and $\nu''_{i,r}$ are the stoichiometric coefficients of reactants and products, and $C_i = \rho Y_i/\mathcal{M}_i$ denotes the molar concentration.

The forward rate constants are written using an extended Arrhenius-type expression:

$$k_{f,r} = A_{f,r} T_{f,r}^{N_{f,r}} \exp\left(-\frac{B_{f,r}}{R T_{f,r}}\right)$$
 (15)

HiSST-2025-244 Copyright © 2025 by the author(s) where $T_{f,r}$ is the effective temperature for the forward reaction, $A_{f,r}$ is the pre-exponential factor, $N_{f,r}$ is the temperature exponent, $B_{f,r}$ is the activation energy, and R is the universal gas constant. The backward rates, assuming reversible reactions, can be obtained by a balance with the reaction equilibrium constant, K_{eq}

$$k_{b,r} = k_{f,r}(T_{b,r})/K_{eq}(T_{b,r})$$
 (16)

In this work, three different 11-species ionizing air kinetic schemes are compared: the scheme proposed by Park in 1985 [14](hereafter referred to as the Park'85 scheme, consisting of 45 elementary reactions), its improved version from 1993 [19](the Park'93 scheme, including 49 reactions), and the more recent formulation proposed by Kim in 2021[10] (the Kim scheme, also with 49 reactions).

Equilibrium constants are generally calculated according to the thermodynamic equilibrium theory from the thermodynamic properties in pressure units:

$$K_{\mathsf{eq},r} = \exp\left(\frac{\Delta S_k^{\circ}}{R} - \frac{\Delta H_k^{\circ}}{RT}\right) \left(\frac{p_{\mathsf{atm}}}{RT}\right)^{\sum_i \nu_{ik}}. \tag{17}$$

For the Park schemes, the equilibrium constant of reaction r, denoted $K_{\rm eq,}$, is instead expressed as a fourth-order polynomial in Z=10000/T. The polynomial coefficients were determined by Park[14] through fits of spectroscopic data:

$$K_{\mathrm{eq},r}(T) = \exp\!\left(A_{1r} + A_{2r}T + A_{3r}T^2 + A_{4r}T^3 + A_{5r}T^4\right).$$

By contrast, the Kim scheme provides the equilibrium constants through different curve-fitted expressions of the form

$$K_{\text{eq},r} \exp(B_{1r}/Z + B_{2r} + B_{3r} \ln Z + B_{4r}Z + B_{5r}Z^2),$$
 (18)

where the fitting parameters are derived from a first-principles statistical-thermodynamics analysis, accounting for electronic, vibrational, and rotational partition functions.

2.2.1. Chemistry vibration coupling

A key aspect of high-enthalpy kinetics is the coupling between chemistry and vibrational energy. Vibrationally excited states can significantly enhance dissociation rates, while dissociation and recombination processes modify the vibrational energy content of the mixture.

This mutual interaction, referred to as chemical—vibrational coupling, is consistently accounted for in the present non-equilibrium framework. In practice, this coupling is introduced at the kinetic level by including the vibrational temperature in the definition of the controlling temperature for selected reactions. The definition of the effective temperature controlling forward and backward reaction rates varies among different kinetic models. Table 1 summarizes the temperatures adopted in the Park'84 and Park'93 formulations, with the Kim scheme considered consistent with Park'93. For each reaction class, the table reports the effective temperature used in the evaluation of both the forward and backward rate coefficients. In the model proposed by Park[14, 15, 16], and here extended also to Kim kinetic schemes, the forward rate coefficient for dissociation reactions is expressed as a function of an effective temperature obtained from the geometric average of the translational temperature T and the vibrational temperature T0, namely

$$T_{a,k} = T^n T_{Vk}^{1-n} (19)$$

which reflects the joint contribution of translational and vibrational energy of the species k to bond breaking. In a two-temperature framework, the effective temperature is unique and depends only on the single vibrational temperature representative of all molecular species, whereas in a multi-temperature framework it becomes reaction-specific, with $T_{v,k}$ selected according to the vibrational mode(s) of the species directly involved in that reaction. On the other hand, the backward rate is controlled only by the translational temperature. For electron impact dissociation, the forward rate is controlled by the vibrational temperature $T_{V,k}$, while the backward rate is governed by the effective temperature $T_{a,k}$. In the case of electron impact ionization, the electron temperature T_{e} is employed when available; otherwise, as in the NExT model, an equivalent vibrational temperature $T_{v,eq}$ is used.

	Pai	rk′85	Park'93, Kim		
	Forward	Backward	Forward	Backward	
Dissociation	$T_{a,k}$	T	$T_{a,k}$	T	
Electron impact dissociation	$T_{V,k}$	$T_{a,k}$	$T_{V,k}$	$T_{a,k}$	
Neutral exchange	$T_{a,k}$	T	T	T	
Associative ionization	T	T	T	T	
Electron impact ionization ¹	T_e	T_e	T_e	T_e	
Charge exchange	$T_{a,k}$	T	T	T	

Table 1. Effective temperature for forward and backward reactions for Park'84,

3. Geometry and Numerical Set-up

The geometry selected for the present study is that of the RAM-C II vehicle, consisting of a hemispherical nose with a radius of approximately 15 cm followed by a 9° half-angle cone, for a total length of about 1.3 m. This simple hemisphere-cone configuration provides a well-defined test case that can be accurately reproduced in numerical simulations while still capturing the essential physical features of hypersonic reentry flows. The choice of RAM-C II is further motivated by the limited availability of experimental data in the literature concerning electron density distributions during atmospheric entry. Among the very few in-flight experiments that reported such measurements, RAM-C II stands out as the most comprehensive, providing both microwave reflectometry antennas (L, S, X, and Ka bands) and electrostatic probe rakes, as illustrated in Fig. 1. These diagnostics delivered valuable information on the spatial and temporal evolution of electron concentration in both the nose and aft regions of the vehicle, making it an indispensable benchmark for validating numerical models and motivating the present numerical investigation.

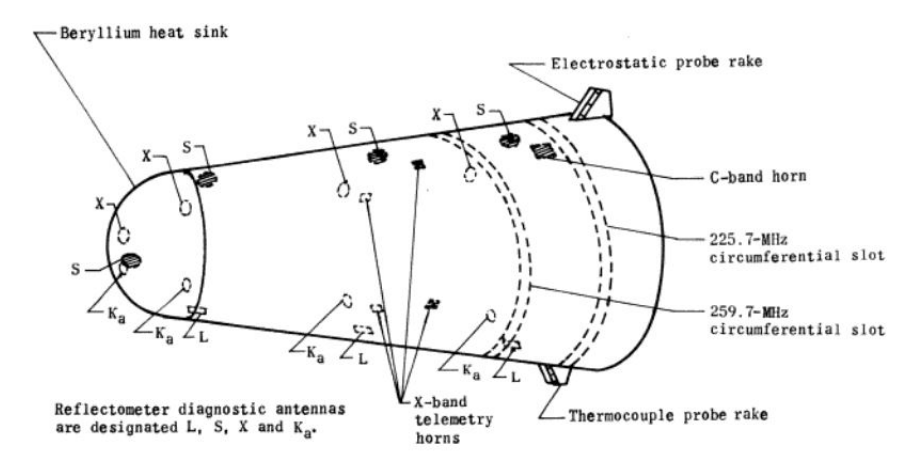


Fig 1. Schematic of the RAM-C II reentry vehicle with diagnostic instrumentation. Image reproduced from [8].

Building on this geometry, the present study initially aimed to assess the predictive capability of the in-house solver NExT by comparing its electron concentration predictions with those obtained using the commercial solver CFD++ and the available experimental data. Both solvers consider a compressible, chemically reacting air mixture in thermal and chemical nonequilibrium, consisting of 11 species: O₂, N_2 , O, N, NO, NO^+ , N_2^+ , O_2^+ , O_2^+ , O_2^+ , O_2^+ , and electrons. In both codes, transport properties are evaluated using the Gupta-Yos formulation [7], where viscosity, thermal conductivity, and binary diffusion coeffi-

HiSST-2025-244

^[1] T_e is taken equal to the single vibrational temperature T_V in a two-temperature framework, or to an equivalent value $T_{V,eq}$ defined by $\sum_i e_{v,i} = \sum_i (\rho_i R \theta_i^v) / (e^{\theta_i^v/T_{V,eq}} - 1)$ in a multi-temperature framework.

Table 2. Flight conditions for RAM-C II at different altitudes.

Altitude	Velocity	ρ	p	T	a	M	T_{wall}
[km]	[m/s]	$[kg/m^3]$	[Pa]	[K]	[m/s]	[-]	[K]
61	7651	$2.5355 \cdot 10^{-4}$	17.66060	242.65	312.273	24.501	1000
71	7660	6.4211 $\cdot 10^{-5}$	3.95642	214.65	293.587	26.091	1000
76	7655	2.98135 ⋅10 ⁻⁵	1.75140	204.65	286.666	26.704	1000
81	7650	$1.33205 \cdot 10^{-5}$	0.74428	194.65	279.575	27.363	1000

cients are obtained from collision integrals based on species collision cross-sections, with corrections for charged-species collisions. The ambipolar diffusion fluxes are computed as done in [21], which enforces mass-flux conservation and couples electron and ion diffusion to preserve charge neutrality in weakly ionized plasmas. All simulations are axisymmetric, with boundary conditions and flight parameters corresponding to RAM-C II conditions summarized in Table 2.

NExT solves the full compressible Navier–Stokes equations coupled with a multi-temperature model for vibrational energy and chemical non-equilibrium. Spatial discretization is based on a finite-volume method using a second-order FDS scheme[13], whereas time integration is performed by employing an explicit multistage Runge-Kutta algorithm coupled with an implicit evaluation of the source terms[4]. NExT is interfaced with both the Gas-Phase Kinetics module of the Chemkin-II [9] package and the VKI Mutation++ chemistry library [22], which serve as external solvers for the evaluation of reaction rates and transport properties in generic reacting gas mixtures governed by a prescribed kinetic scheme. Chemkin-II is restricted to systems under thermal equilibrium, i.e., it assumes a single temperature for translational, vibrational, and electronic energy modes. In contrast, Mutation++ is capable of handling non-equilibrium, multi-temperature formulations, thereby extending the range of applicability to more complex thermochemical environments. Furthermore, Mutation++ incorporates multiple transport models for the evaluation of viscosity and thermal conductivity, including the Gupta–Yos semi-empirical [7] formulation and the rigorous Chapman–Enskog solution. Chemkin-II, on the other hand, provides only transport models derived from kinetic theory at the pure species, with mixture properties computed via Wilke's rule.

CFD++, developed by Metacomp Technologies [3], solves the same governing equations but adopts a two-temperature (2-T) model, in which the vibrational, electronic, and electron degrees of freedom are grouped into a single effective temperature, T_{ve} [18]. Upwind fluxes are computed using a HLLC Riemann solver, while time integration is carried out with an implicit scheme [20]. The simulations in CFD++ were performed assuming a non-catalytic wall, with free-stream and inflow/outflow boundary conditions consistent with those adopted in NExT

After establishing the benchmark comparison between NExT and CFD++, further studies were conducted to systematically evaluate the solver's sensitivity to different modeling parameters. These included extending the comparison to Park'85 and Kim kinetic schemes in addition to Park'93, assessing the impact of wall boundary conditions (non-catalytic walls, fully catalytic treatment for charged species only, and fully catalytic walls for all species), examining the influence of equilibrium constants computed either via Gibbs free energy minimization or using the fitting formulas provided by Park'93 and Kim, and evaluating the effect of chemical–vibrational coupling by varying the definition of the controlling temperature T_a across the flight conditions listed in Table 2.

4. Results

This section presents a comparison between numerical predictions and RAM-C II flight data [8], aimed at evaluating the capability of different physical models to replicate the measured plasma environment. The analysis is structured to progressively isolate the main sources of uncertainty in hypersonic reentry simulations. First, the influence of the numerical solver is assessed by comparing results from NExT and CFD++. The baseline performance of the NExT solver is then evaluated across a range of flight conditions. Subsequently, the role of chemical kinetics is examined through comparisons of various reaction

mechanisms, followed by an investigation of the influence of wall catalysis. This approach enables a structured assessment of how solver formulation, kinetic modeling, and boundary conditions affect the fidelity of plasma flow simulations.

Fig. 2 compares electron density profiles obtained using NExT (solid lines) and CFD++ (dashed lines) against RAM-C II flight measurements (symbols). Two chemical kinetic schemes are considered: Park'93 (top row) and Kim (bottom row), evaluated at three altitudes—61 km (red), 71 km (blue), and 81 km (black). The computation of reaction rates relies on thermodynamic equilibrium theory.

The results indicate that solver discrepancies are most pronounced at the lowest (61 km) and highest (81 km) altitudes. At 71 km, both solvers yield reasonable agreement with experimental data. NExT demonstrates relatively limited sensitivity to the choice of kinetic model, maintaining consistent accuracy in both the magnitude and decay rate of electron density with increasing altitude. In contrast, CFD++ exhibits a stronger dependence on the chemical mechanism, with significantly improved accuracy when using the Kim model across all altitudes. One cause of these discrepancies is the different wall boundary conditions. Simulations in CFD++ are performed considering a non-catalytic wall, which, as shown in the results below, tends to overestimate the electron density. NExT, by contrast, applies a wall condition in which only neutral species are non-catalytic, while charged species are fully catalytic. Another contributing factor is the different solvers' physical formulations. CFD++ employs a two-temperature (2-T) approach, grouping vibrational, electronic, and electron energies into a single effective temperature, T_{vel} whereas NExT resolves vibrational energy modes separately using a multi-temperature model. This distinction becomes critical when chemical-vibrational coupling is significant, as the characteristic temperatures governing reaction rates can differ substantially from the translational-rotational temperature, and the wall interaction significantly affects electron density predictions.

Fig. 3 shows the effect of different treatments of ionization chemistry and vibration—chemistry coupling on the predicted distribution of number density along the payload, as resolved by NExT. The red curves correspond to solutions obtained with the Chemkin-II (CK) and Mutation++ (MPP) chemistry libraries using the standard approach, i.e., adopting the translational temperature for reaction rate evaluation and equilibrium constants from classical thermodynamic equilibrium theory. Although the two libraries produce results in close agreement, both systematically over-predict the electron number density across the entire configuration. Improved agreement is obtained when employing the equilibrium constant fit proposed by Park and later refined by Kim (blue curve). However, only with the inclusion of vibration-chemistry coupling-implemented in this work by assigning the appropriate temperature for rate calculations, as described in Section 2.2.1—do the predictions converge satisfactorily with the experimental data, as evidenced by the green curve.

Fig. 4 presents electron number density profiles computed with NExT under various flight conditions, using Park'93 reaction rates with fitted equilibrium constants. The left panel shows the evolution of peak electron density along the payload. Across all altitudes—61 km (red), 71 km (blue), 76 km (green), and 81 km (black)—the simulations accurately reproduce the experimental trends, capturing both the overall decay and the correct order of magnitude. Agreement with the data is consistent along the payload, with only minor amplitude deviations.

The right panel displays the electron density distribution in the aft region, along a direction of approximately 45° from the wall. The solver correctly predicts the altitude-dependent decrease in electron density and replicates the qualitative behavior observed in flight data. At 61 km, the predicted values approach the saturation threshold of the measurement system. At higher altitudes, a slight overprediction near the wall is observed, likely due to the absence of the electrostatic rake probe in the computational geometry. The interaction between the probe and the surrounding flow may generate local shockwaves that affect the electron density distribution, contributing to the observed discrepancies.

Fig. 5 examines the sensitivity of peak electron number density along the payload to the chemical kinetic model, across four altitudes. Comparisons are made among the Park'85, Park'93, and Kim models. Park'85 consistently overestimates electron density, particularly at lower altitudes. Park'93 and Kim, in contrast, yield similar results and generally provide better agreement with experimental data. As altitude increases, differences between models diminish due to the reduced density and pressure, which slow down ionization and recombination processes and reduce the influence of kinetic rates.

HiSST-2025-244 Copyright © 2025 by the author(s)

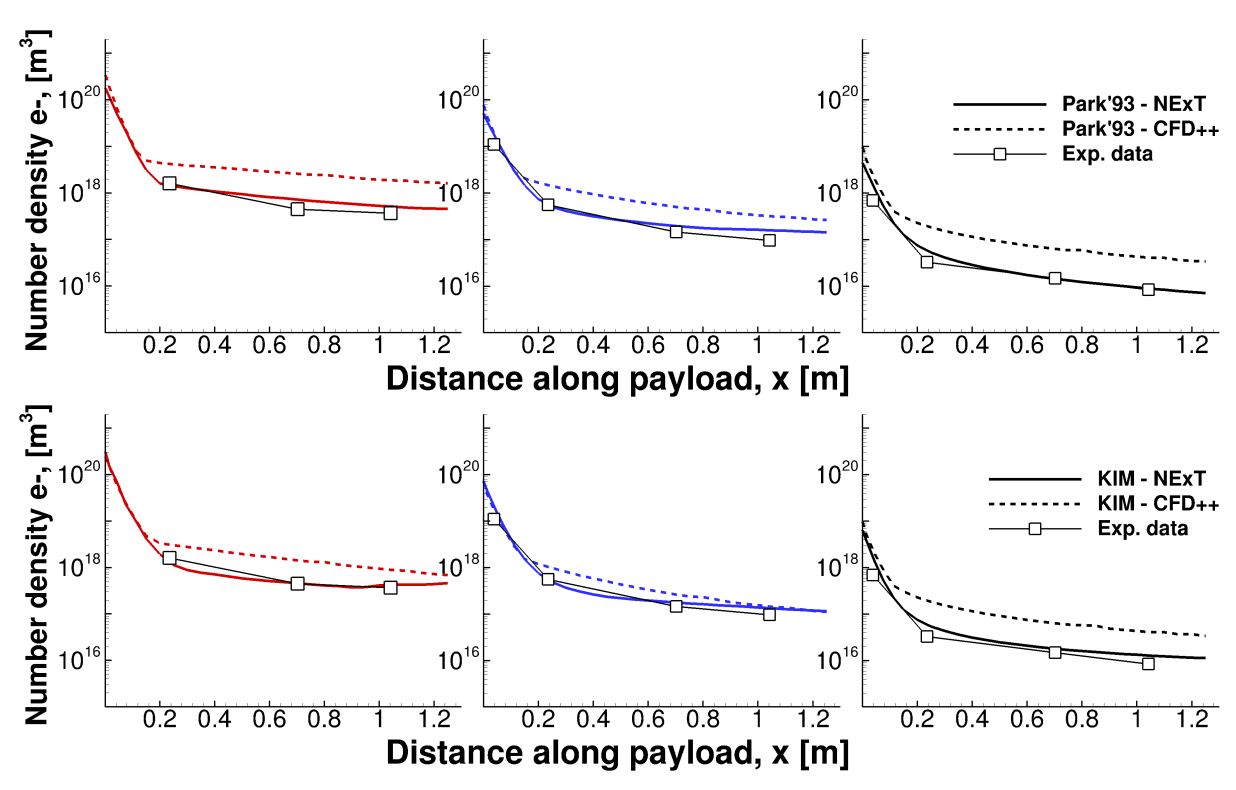


Fig 2. Comparison between NExT and CFD++ results: number density profile along the payload assuming Park'93 (top) and Kim (bottom) kinetic schemes and equilibrium reaction constant by thermodynamic equilibrium theory. Colors: red = 61 km, blue = 71 km, black = 81 km.

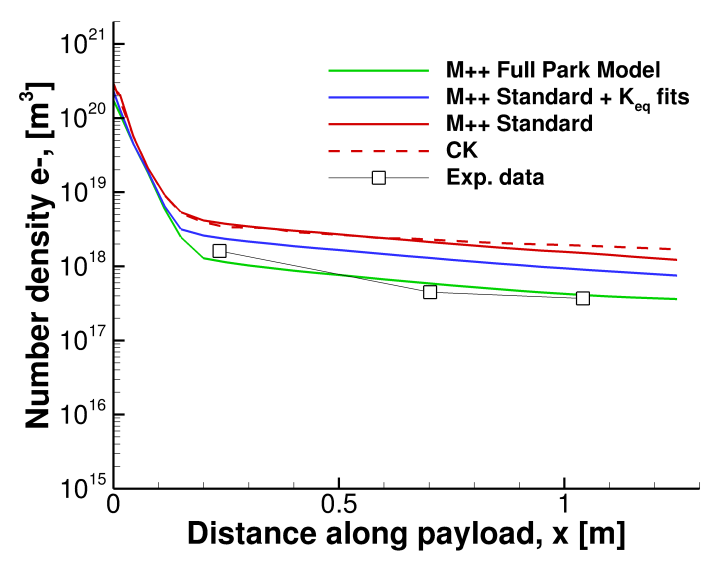


Fig 3. Comparison of electron number density distributions obtained with Chemkin-II (CK) and Mutation++ using equilibrium-based rate formulations (red), Park–Kim equilibrium constant correlation (blue), and full vibration—chemistry coupling (green).

Fig. 6 illustrates mass fraction profiles of neutral species along the stagnation line at various altitudes. The most significant differences between chemical models are observed at lower altitudes, affecting

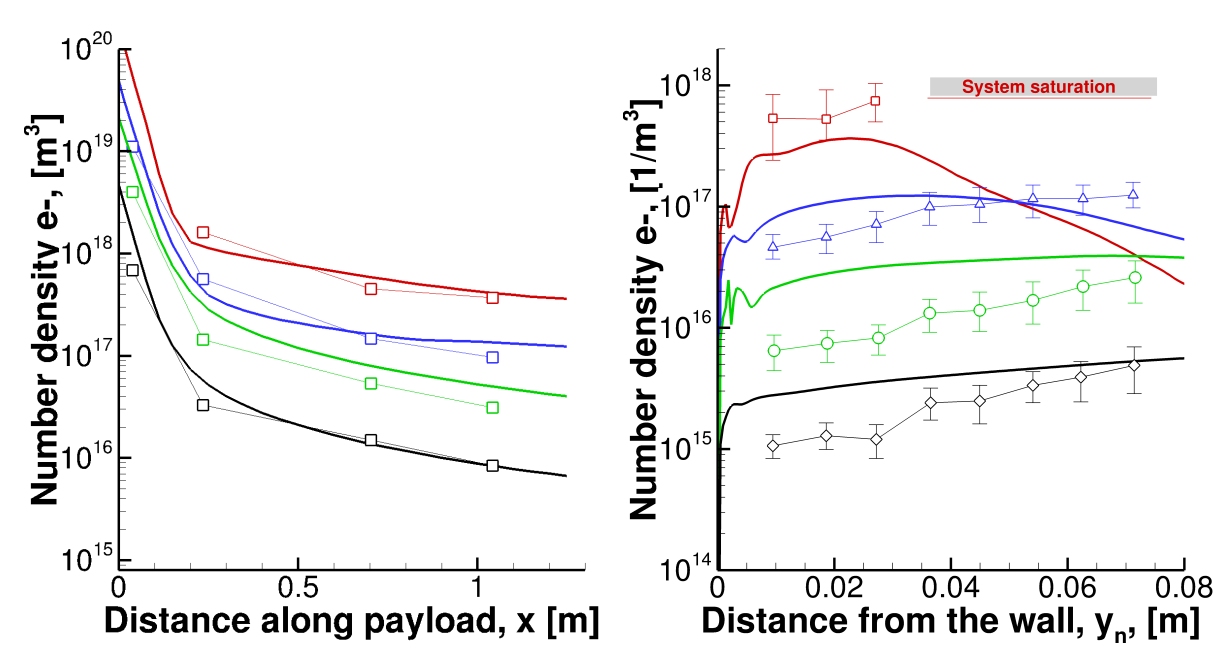


Fig 4. Electron number density profiles: (left) peak distributions along the payload; (right) boundary-layer profiles in the aft region. Lines: CFD (NExT baseline); symbols: flight measurements. Colors: red = 61 km, blue = 71 km, green = 76 km, black = 81 km.

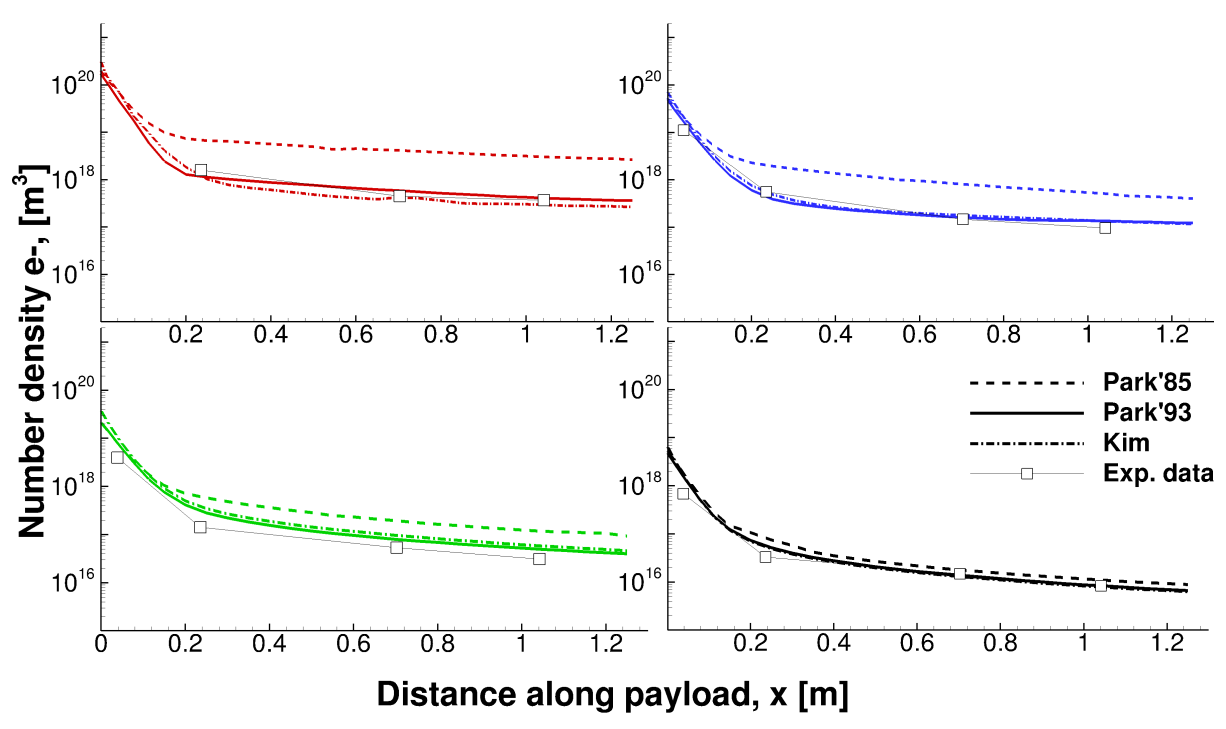


Fig 5. Effects of chemical kinetics on the electron number density peaks profiles. —: Park'93, ---: Park'85, ---: Kim. Colors: red = 61 km, blue = 71 km, green = 76 km, black = 81 km.

both the shock layer structure and species distribution. The Kim model predicts a larger stand-off distance, positioning the shockwave further from the surface. Park'93 leads to more extensive dissociation

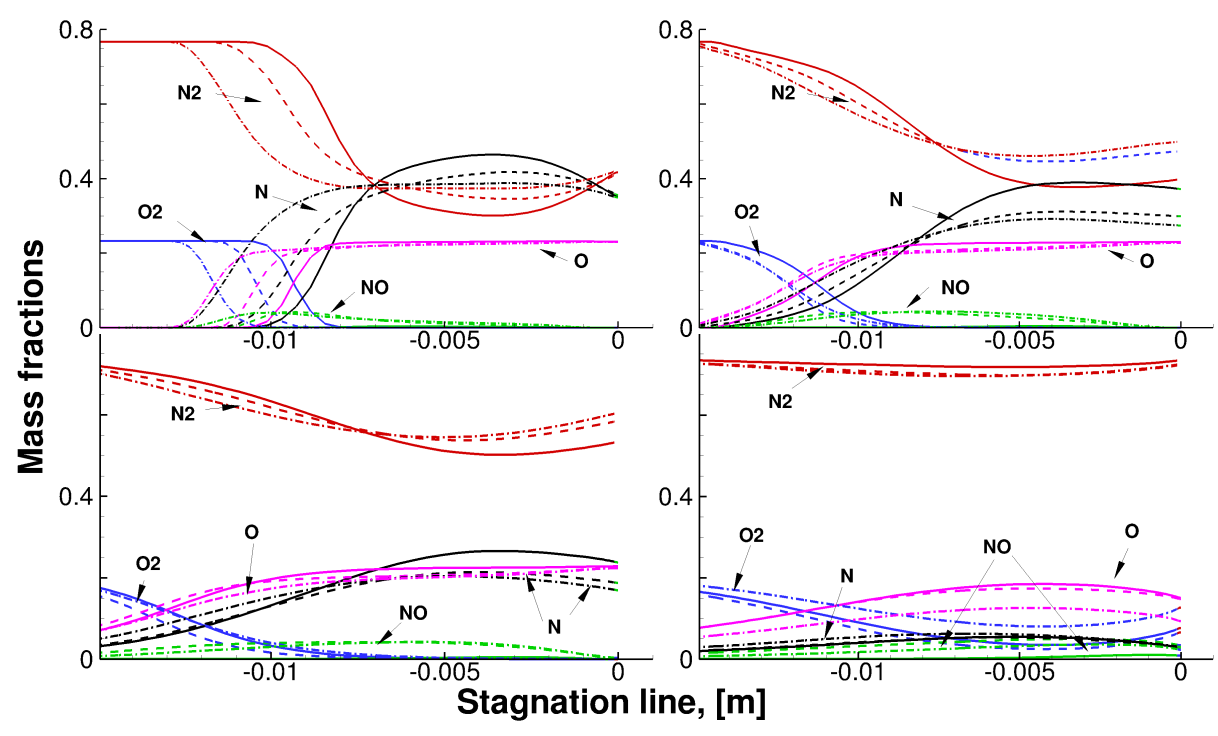


Fig 6. Effects of chemical kinetics on the species profiles along the stagnation line —: Park'93, ---: Park'84, ---: Kim. Colors: red = N_2 , blue = N_2 , green = N_2 , blue = N_2 , blue

of N_2 and O_2 , while both Kim and Park'85 result in higher NO formation. These distinctions, however, become less significant at higher altitudes, as lower densities suppress thermochemical activity and reduce sensitivity to the specific kinetic mechanism.

Fig. 7 depicts the impact of wall catalysis modeling on the electron density distribution along the RAM-C II payload. Three boundary conditions are considered: non-catalytic (NC), fully catalytic (FC), and a "hybrid" catalytic configuration in which neutral species are treated as non-catalytic while charged species undergo full catalytic recombination. Across all altitudes investigated (61, 71, 76, and 81 km), the NC model (dashed lines) consistently overpredicts electron densities relative to the flight data, whereas the FC model (dash-dotted lines) tends to underestimate them. The intermediate case (solid lines) yields predictions that generally fall between these two limits and offers the closest agreement with experimental measurements. Although some quantitative variations emerge with altitude, the qualitative influence of surface catalyticity remains consistent. These results indicate that adopting a "hybrid" catalytic boundary condition provides a more realistic representation of the RAM-C II plasma environment, while the limiting cases lead to systematic over- or underestimation.

5. Conclusions

A comparative analysis was conducted to evaluate the sensitivity of electron density predictions in hypersonic reentry flows to various modeling assumptions and solver implementations. Numerical simulations were performed using the in-house solver NExT and compared against results from the commercial code CFD++, with experimental data from the RAM-C II flight campaign serving as reference.

The comparison between solvers showed that NExT and CFD++ generally agree at intermediate altitudes, while larger discrepancies arise at the highest and lowest altitudes investigated. These differences were observed to depend on the underlying chemical kinetic model, with the Kim scheme producing better agreement with experimental data in CFD++ simulations at high altitude.

When evaluated independently, NExT accurately reproduced the trend and order of magnitude of elec-

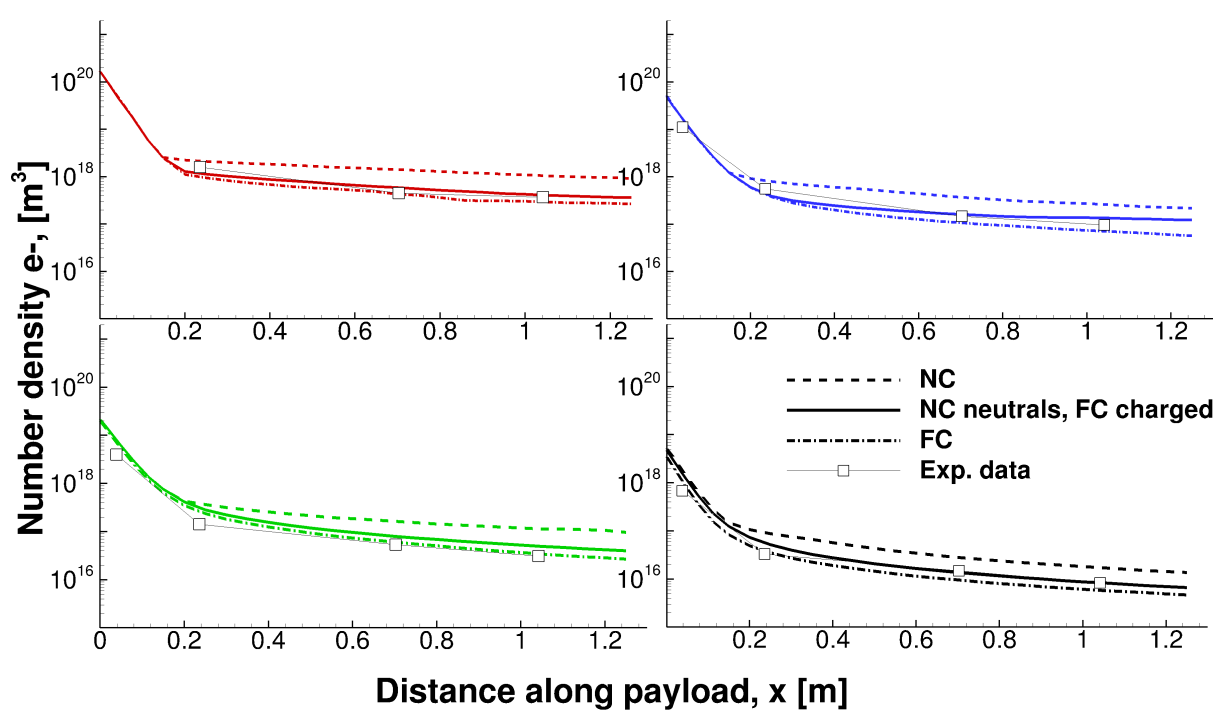


Fig 7. Effects of wall catalysis modeling. ---: Non-catalytic (NC), --: Non-catalytic for neutral and fully-catalytic for charged species, ---: Fully-catalytic (FC). Colors: red = 61 km, blue = 71 km, green = 76 km, black = 81 km.

tron densities along the payload at all altitudes considered. Deviations in the aft region were noted and attributed to geometric simplifications in the simulation setup.

Chemical kinetics were identified as a relevant source of variation. Among the three reaction mechanisms tested, Park'85 consistently led to higher electron densities, particularly at low altitudes, while Park'93 and Kim yielded similar predictions that aligned more closely with the experimental data. Differences among models became less pronounced at higher altitudes.

Species profiles along the stagnation line confirmed that chemical kinetics influences shock layer structure and dissociation behavior. Notable distinctions in species distributions were observed at lower altitudes, while reduced differences were found at higher altitudes.

Wall catalysis was shown to significantly affect predicted electron densities. Fully catalytic and non-catalytic boundary conditions led to under- and overprediction, respectively. A hybrid treatment—non-catalytic for neutral species and fully catalytic for charged species—resulted in the closest match with measured profiles across all conditions studied.

Overall, the results highlight the relative impact of solver formulation, chemical kinetics, and surface boundary conditions on the numerical prediction of plasma properties during atmospheric reentry, within the specific test case and modeling framework considered.

6. Acknowledgements

The authors gratefully acknowledge Alessio Improta for his assistance in performing the CFD++ simulations, which were essential to this study.

References

- [1] John D. Anderson. Hypersonic and High Temperature Gas Dynamics. American Institute of Aeronautics and Astronautics, Reston, VA, 3rd edition, 2019.
- [2] Nathan Blaunstein and Eugeniu Plohotniuc. Ionosphere and applied aspects of radio communication

- and radar. CRC press, 2008.
- [3] Sukumar Chakravarthy, Oshin Peroomian, Uriel Goldberg, and Sampath Palaniswamy. The cfd++ computational fluid dynamics software suite. In AIAA and SAE, 1998 World Aviation Conference, page 5564, 1998.
- [4] L. Cutrone, M. Tuttafesta, M. Capitelli, A. Schettino, G. Pascazio, and G. Colonna. 3D nozzle flow simulations including state—to—state kinetics calculation. In AIP Conference Proceedings, volume 1628, pages 95–102, December 2014.
- [5] Salvatore Esposito, Domenic D'Ambrosio, et al. A study on plasma formation on hypersonic vehicles using computational fluid dynamics. In Proceedings of the Aerospace Europe Conference 2023–10TH EUCASS–9TH CEAS. EUCASS, 2023.
- [6] Salvatore Esposito, Andrea Scarabosio, Giuseppe Vecchi, and Domenic D'Ambrosio. Nonequilibrium plasma distribution in the wake of a slender blunted-nose cone in hypersonic flight and its effect on the radar cross section. Aerospace Science and Technology, 155:109699, 2024.
- [7] R. N. Gupta, J. M. Yos, R. A. Thompson, and K-P. Lee. A review of reaction rates and thermodynamic and transport properties for an 11-species air model for chemical and thermal nonequilibrium calculations to 30000 K. 1990.
- [8] W. Linwood Jones and Aubrey E. Cross. Electrostatic-Probe Measurements of Plasma Parameters for Two Reentry Flight Experiments at 25,000 Feet per Second. Technical Report 6617, NASA, 1972.
- [9] Robert J. Kee. Chemkin-ii: A fortran chemical kinetics package for the analysis of gas phase chemical kinetics. 1991.
- [10] Jae Gang Kim and Sung Min Jo. Modification of chemical-kinetic parameters for 11-air species in re-entry flows. International Journal of Heat and Mass Transfer, 169:120950, 2021.
- [11] L. D. Landau and E. Teller. Zur theorie der schallabsorption in festkörpern. Physikalische Zeitschrift der Sowjetunion, 10:34–43, 1936.
- [12] Roger C. Millikan and Donald R. White. Systematics of vibrational relaxation. The Journal of Chemical Physics, 39(12):3209–3213, 12 1963.
- [13] M. Pandolfi and S. Borrelli. An Upwind Formulation for Hypersonic Non-equilibrium Flows. Modern Research Topics in Aerospace Propulsion. Springer-Verlag, 1991.
- [14] C. Park. On the convergence of computation of chemically reacting flows. In 23^{rd} AIAA Aerospace Sciences Meeting and Exhibit, Reno, NV, January 1985. AIAA. AIAA Paper 1985-0247.
- [15] C. Park. Assessment of two temperature kinetic model for dissociating and weakly-ionizing nitrogen. In 4th Joint Thermophysics and Heat Transfer Conference, Boston, MA, June 1986. AIAA. AIAA Paper 1986-1347.
- [16] C. Park. Assessment of two temperature kinetic model for ionizing air. In 22nd Thermophysics Conference, Honolulu, HI, June 1987. AIAA. AIAA Paper 1987-1574.
- [17] C. Park and S. H. Lee. Validation of multi-temperature nozzle flow code noznt. In 28^{th} AIAA Thermophysics Conference, Orlando, FL, July 1993. AIAA. AIAA Paper 1993-2862.
- [18] Chul Park. Assessment of two-temperature kinetic model for ionizing air. Journal of thermophysics and heat transfer, 3(3):233–244, 1989.
- [19] Chul Park. Review of chemical-kinetic problems of future NASA missions. i earth entries. Journal of Thermophysics and Heat Transfer, 7(3):385–398, 1993.

- [20] Oshin Peroomian, Sukumar Chakravarthy, Sampath Palaniswamy, and Uriel Goldberg. Convergence acceleration for unified-grid formulation using preconditioned implicit relaxation. In 36th AIAA Aerospace Sciences Meeting and Exhibit, page 116, 1998.
- [21] Leonardo C Scalabrin. Numerical simulation of weakly ionized hypersonic flow over reentry capsules. PhD thesis, University of Michigan., 2007.
- [22] James B. Scoggins, Vincent Leroy, Georgios Bellas-Chatzigeorgis, Bruno Dias, and Thierry E. Magin. Mutation++: Multicomponent thermodynamic and transport properties for ionized gases in c++. SoftwareX, 12, 2020.
- [23] Surendra P. Sharma, Winifred M. Huo, and Chul Park. Rate parameters for coupled vibration-dissociation in a generalized ssh approximation. Journal of Thermophysics and Heat Transfer, 6(1):9–21, 1992.
- [24] Hema Singh, Simy Antony, and Rakesh Mohan Jha. Plasma-based radar cross section reduction. Plasma-based radar cross section reduction, pages 1–46, 2015.
- [25] Thomas H Stix. Waves in plasmas. Springer Science & Business Media, 1992.